Letter

Coexistence of local structural heterogeneities and long-range ferroelectricity in Pb-free (1-x)Ba($Zr_{0.2}Ti_{0.8}$)O_3-x($Ba_{0.7}Ca_{0.3}$)TiO_3 ceramics

K. Dey,[1] A. Ahad,[2] K. Gautam,[1] A. Tripathy,[1] S. S. Majid,[2,*] S. Francoual,[3] C. Richter,[4,†] M. N. Singh,[5] A. Sagdeo,[5,6] E. Welter,[3] N. Vittayakorn,[7] V. G. Sathe,[1] R. Rawat,[1] and D. K. Shukla[1,‡]

[1]*UGC DAE Consortium for Scientific Research, University Campus, Khandwa Road, Indore 452001, India*

[2]*Department of Physics, Aligarh Muslim University, Aligarh 202002, India*

[3]*DESY, Notkestrasse 85, D-22607 Hamburg, Germany*

[4]*The European Synchrotron Radiation Facility, 71 Avenue des Martyrs, 38000 Grenoble, France*

[5]*Synchrotrons Utilization Section, Raja Ramana Centre for Advance Technology, Indore 452013, India*

[6]*Homi Bhabha National Institute, Training School Complex, Anushakti Nagar, Mumbai 400094, India*

[7]*Advanced Materials Research Unit, Faculty of Science, King Mongkut's Institute of Technology Ladkrabang, Bangkok, 10520 Thailand*

(Received 9 December 2020; accepted 9 March 2021; published 29 March 2021)

Environmentally benign (1-x)Ba($Ti_{0.8}Zr_{0.2}$)O_3-x($Ba_{0.7}Ca_{0.3}$)TiO_3 (BZT-BCT) ceramics are promising materials due to their remarkable high piezoresponse [Liu and Ren, Phys. Rev. Lett. **103**, 257602 (2009)]. In this Letter, by focusing on local and average structure in combination with macroscopic electromechanical and dielectric measurements we demonstrate the structure property relationship in the tetragonal BZT-BCT ceramic. During high-temperature cubic to tetragonal phase transformation, polar nanoregions are manifested through the spontaneous volume ferroelectrostriction at temperatures below ~477 K. Temperature-dependent local structural investigations across the Zr K edge extended x-ray absorption fine-structure spectroscopy reveal an anomalous collaboration between the ZrO_6 and TiO_6 octahedra. These octahedra compromise their individuality during polarization development. The presence of domains of submicron size embedded inside the macroscopic ferroelectric regions below T_m, as well as their hierarchical arrangement, is observed by piezoresponse force microscopy. Effects of the existence of the structural/polar heterogeneities below T_m are observed also when polarizabilities of the poled and unpoled samples are compared; the poled sample is found to be more susceptible to the electric field. In addition, by using electric field dependent x-ray diffraction studies we also show that this ceramic under field exhibits a reduction of tetragonal distortion, which is consistent with earlier reports.

DOI: 10.1103/PhysRevB.103.L100205

I. INTRODUCTION

Investigations on lead-free piezoelectric materials in the last two decades have largely intensified due to environmental concerns. Liu and Ren [1] demonstrated a $PbZr_xTi_{1-x}O_3$ (PZT) like "morphotropic phase boundary" (MPB) starting from a triple point in (1-x)Ba($Ti_{0.8}Zr_{0.2}$)O_3-x($Ba_{0.7}Ca_{0.3}$)TiO_3 (BZT-BCT) which possesses ultrahigh piezoresponse (d_{33} values as high as up to 560–620 pC/N) among all lead-free compositions. From Liu and Ren [1] and Nahas *et al.* [2], high piezoresponse has been attributed to isotropic energy flattening along with miniaturization of domains towards the triple point [3]. In addition, domain wall motion was reported to be the dominant extrinsic contribution to high piezoresponse [4]. Electric field dependent x-ray diffraction (XRD) measurements [5] revealed that spontaneous lattice strain reduction enhances domain wall motion in BZT-BCT ceramics. In a morphotropic composition (BZT-50BCT) Brajesh *et al.* [6,7] showed phase coexistence at room temperature (tetragonal+rhombohedral+orthorhombic) and concluded that electric field induced metastable phases contribute significantly to high piezoresponse. They also showed relaxor ferroelectric behavior and an ergodic relaxor to normal ferroelectric transformation at $\sim T_m$. Relaxor ferroelectricity, i.e., the existence of polar nanoregions (PNRs), a nanoscale inhomogeneity, has been prototypical of the highest piezoresponse in Pb-based materials [8–10]. However, in BZT-BCT ceramics, among all possibilities of high piezoresponse discussed so far, thorough validation of PNRs is yet missing.

In Pb-based perovskite relaxor ferroelectrics, the quenched compositional disorder induced by heterovalent substitution at the B site (e.g., $Pb(Mg_{1/3}Nb_{2/3})O_3$-$PbTiO_3$, $Pb(Zn_{1/3}Nb_{2/3})O_3$-$PbTiO_3$) generates random fields which break long-range ferroelectricity, and frustrated interactions among dipoles start to form nanoscale correlations (PNRs) at a higher temperature which is known as the characteristic Burn's temperature T_B [11,12]. Furthermore, the effect of the Pb positional disorder and its coupling with different BO_6 octahedra also plays a critical role [13,14]. The PNRs exhibit a large distribution of relaxation times. Divergence of the longest relaxation time takes place at a characteristic temperature, T_f, the

*Now at Institute of Earth Sciences, Academia Sinica, Taipei 115201, Taiwan.

†Now at Leibniz-Institut für Kristallzüchtung, Max-Born-Strasse 2, 12489 Berlin, Germany.

‡Corresponding author: dkshukla@csr.res.in

freezing temperature [15]. In the ergodic relaxor phase, between two characteristic temperatures (T_B and T_f) PNRs have intrinsic dynamic character, and after some percolation limit they transfer into ferroelectric domains just below T_f where macroscopic symmetry changes. However, in the case of canonical relaxors (for, e.g., PMN), the macroscopic symmetry remains the same during ergodic to nonergodic transition, and PNRs show glassy interactions among dipoles in the nonergodic relaxor phase which transform into ferroelectric domains upon the application of sufficiently large electric field [16].

$BaTiO_3$-based compositions (e.g., $BaZr_xTi_{1-x}O_3$, $BaSn_xTi_{1-x}O_3$, $BaHf_xTi_{1-x}O_3$) exhibit broad dielectric permittivity maxima with frequency dispersion and characteristic temperatures (T_B and T_f) similar to those in Pb-based relaxors [17,18], and in these compositions also the possible existence of PNRs has been reported [19,20]. However, the origin of PNRs in homovalent substituted $BaTiO_3$-based compositions is different than in Pb-based compositions (as explained above) and challenging to unravel. A pair distribution function study [21] of BZT ($BaZr_xTi_{1-x}O_3$) revealed dynamic insights and highlighted the role of Zr in slowing down the B site (Ti) dynamics (responsible for PNR formation). Therefore, in order to have deeper insights into PNRs in BZT-BCT ceramics it is pivotal to have local structural information about the Zr/Ti ions.

We have chosen a tetragonal composition $[(Ba_{0.82}Ca_{0.18})(Ti_{0.92}Zr_{0.08})O_3$ (BZT-60BCT)] among the BZT-BCT systems mainly because it is far from the triple point and morphotropic composition. In compositions near the triple point and MPB, structural instabilities due to the presence of metastable orthorhombic phases [7,22] and nearly vanishing anisotropy induced domain wall motion [5] may inhibit the study of intrinsic features of PNRs, which are hiding in these ceramics.

In this Letter, we demonstrate that, in BZT-60BCT below T_m, local structural heterogeneities coexist with long-range ferroelectricity, and this coexistence leads to hierarchical arrangements of micro- and nanodomains inside large ferroelectric domains. We also show direct evidence of PNRs above T_m. Our detailed local structural studies of TiO_6 and ZrO_6 reveal a peculiar behavior of these two octahedra during polarization development and static disorder in Zr-O bonds below T_m.

II. EXPERIMENTS

The ceramic BZT-60BCT has been synthesized by conventional solid-state reaction using high-purity chemicals: $BaCO_3$ (99.9%), $CaCO_3$ (99.9%), TiO_2 (99.9%), and ZrO_2 (99.7%). Stoichiometrically mixed powders were thoroughly ball milled and calcined at 1300 °C for 4 h. Sintering was performed at ∼1540 °C for 2 h in air. Dielectric measurements were performed utilizing a Hioki LCR meter (IM 3536) and a CRYOCON temperature controller. Polarization-electric field (P-E) hysteresis loops were measured by a Radiant Precision Premier II loop tracer. Temperature-dependent XRD measurements were carried out at the BL12 beamline at Indus II, Raja Ramana Centre for Advance Technology, India, by utilizing photons of 14.87 keV (0.834 Å) in $\theta - 2\theta$ geometry during the heating cycle from room temperature up to 575 K. The Raman measurements were carried out using a Horiba JY model HR-800 single spectrometer with high-resolution grating and a CCD detector by using a 473-nm laser beam in the backscattering geometry. Electric field dependent x-ray diffraction was performed using high-energy photons (∼37 keV) in the transmission geometry at beamline P09 at PETRA III at DESY (Hamburg, Germany). A PerkinElmer two-dimensional detector was used at a fixed distance of ∼650 mm. For poled measurements, the sample was poled at ∼40°C for 30 min at 1 kV/mm and then field cooled down to room temperature. After ∼24 h of aging of the poled samples, the piezoelectric charge coefficient d_{33} was monitored by a commercial d_{33} meter from American Piezo Ceramics. A similar poling strategy was adopted for all other poled measurements. Extended x-ray absorption fine-structure (EXAFS) measurements at the Zr K edge in transmission and Ti K-edge x-ray absorption near-edge structure (XANES) in fluorescence were collected at P65 beamline of the PETRA III synchrotron. Peizoresponse force microscopy (PRFM) measurements were carried out on mirror-finished polished surfaces. The sample was annealed at 350 °C for 2 h to remove stresses induced by polishing. PRFM measurements were carried out using a fiber interferometry based low-temperature scanning probe microscope system from Attocube. A PtSi-FM conducting cantilever from Nanosensors was used to scan the sample surface. Topography was measured in the contact mode along with simultaneous measurement of the piezoresponse at an applied ac voltage of 10 V (peak to peak) at 41.33 kHz.

III. RESULTS

The room temperature tetragonal structure of BZT-60BCT has been confirmed using XRD (see Fig. S1 in the Supplemental Material [23]). The real and imaginary parts of the dielectric permittivity show diffused dielectric maxima at ∼380 K [see Figs. 1(a) and 1(b)], signatures of relaxor ferroelectricity. Inset (ii) in Fig. 1(b) shows that the inverse permittivity deviates from the Curie-Weiss law at ∼477 K, which indicates a characteristic Burn's temperature T_B [24]. The diffusion exponent γ and diffuseness δ of the permittivity peak are calculated from the fit (see inset (i) in Fig. 1(b)) using an empirical formula from Ref. [25], $\frac{\varepsilon_m}{\varepsilon} = 1 + \frac{(T-T_m)^\gamma}{2\delta^2}$, where T_m is the peak temperature at the selected frequency. Obtained fitting parameters are $\gamma = 1.52$ and $\delta = 8.7$ K. The P-E hysteresis loop in Fig. 1(c) exhibits coercive field $E_C \sim 4$ kV/cm and remanence ∼10 μC/cm^2. The temperature-dependent remanence [see the inset in Fig. 1(c)] is plotted from P-E loop measurements done at various temperatures [23] and shows a nonzero value of polarization even above $T_m \sim 380$ K. The observations of Burn's temperature and nonzero value of polarization above T_m indicate the existence of PNRs at temperatures above T_m. A longitudinal piezoelectric coefficient d_{33} of ∼223 pC/N and its temperature insensitivity up to ∼375 K can be radially seen in Fig. 1(d); the inset shows normalized d_{33} with temperature, and its maximum variation is found to be only ∼8.52%, which is better than the requirement (∼10 %) for applications.

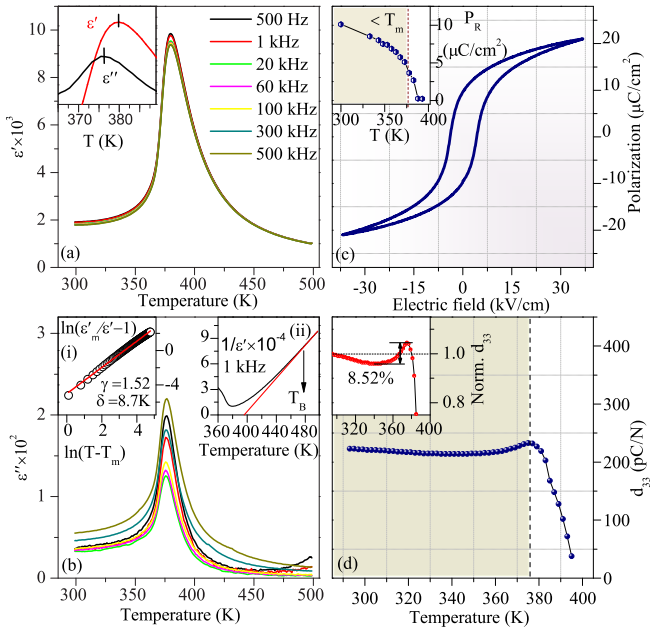

FIG. 1. Temperature dependence of (a) the real and (b) imaginary parts of relative permittivity at different frequencies. The inset in (a) shows the zoomed portion of real and imaginary permittivities near the peak at 1 kHz. The bars indicate that T_m for the imaginary part is at a lower temperature than that of the real part. Inset (ii) in (b) shows that the Curie-Weiss fit of the real permittivity indicates a deviation from the temperature marked T_B (~477 K), and inset (i) in (b) shows the linear fitting by using the empirical formula (see text). (c) Polarization- electric field hysteresis loop at room temperature; the inset shows the temperature dependence of the remnant polarization. (d) Temperature-dependent d_{33}; the inset shows normalized d_{33} with temperature, and the arrow indicates the maximum percentage change in d_{33}.

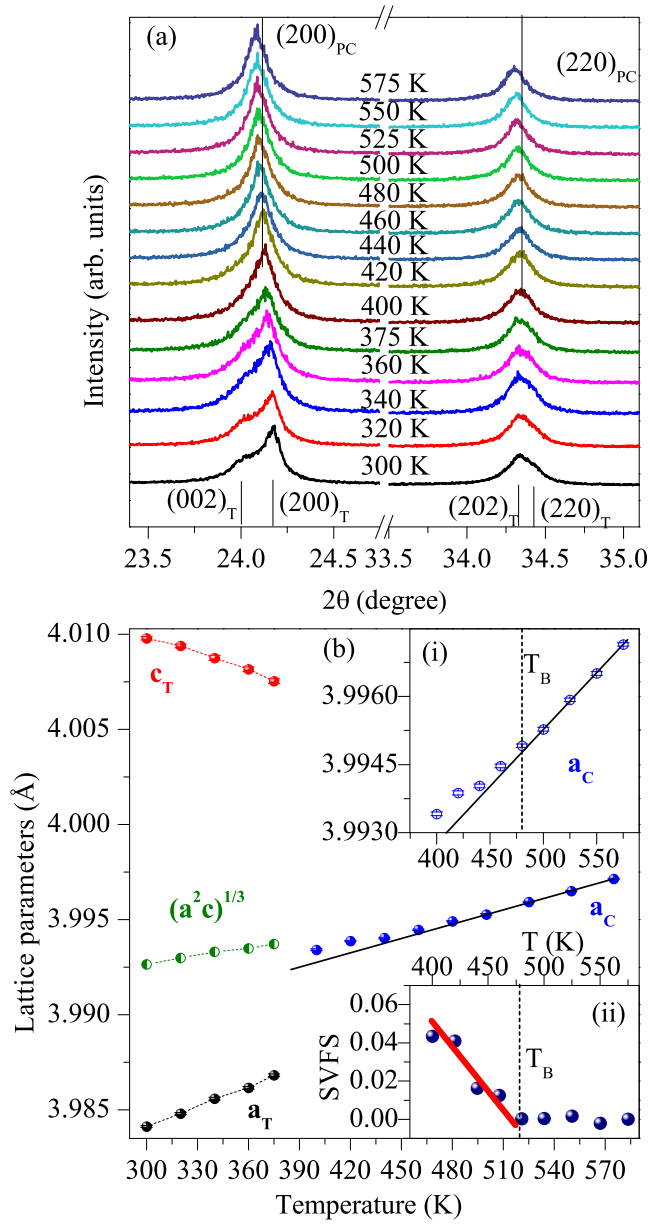

FIG. 2. (a) Temperature dependence of reflections $(200)_{PC}$ and $(220)_{PC}$. (b) Temperature variation of lattice parameters in tetragonal and cubic structures. Inset (i) in (b) shows the zoomed portion of the cubic lattice parameters' temperature dependence. Inset (ii) in (b) shows the calculated spontaneous volume ferroelectrostriction (SVFS) with temperature.

To further substantiate the presence of PNRs and to have insights into the characteristic temperatures (T_B and T_m) observed in macroscopic electrical measurements we now focus on structural study results obtained using synchrotron XRD measurements as a function of temperature (300 to 575 K). Figure 2(a) shows that the high-temperature pseudocubic (PC) reflections $(200)_{PC}$ and $(220)_{PC}$ split with decreasing temperature in $(200)_T/(002)_T$ and $(220)_T/(202)_T$, respectively, signifying a structural phase transition from cubic to tetragonal.

Rietveld refinement is done using the FULLPROF program [26] with space group *P*4*mm* from room temperature to 375 K and with the space group *Pm*-3*m* from 400 up to 575 K (see Fig. S1 in the Supplemental Material [23]). Figure 2(b) shows the temperature dependence of the refined lattice parameters. Transitions in the lattice parameter trend clearly match the dielectric maximum temperature T_m [see Fig. 1(a)]. Interestingly, inset (i) in Fig. 2(b) shows the deviation of the cubic lattice parameters at ~477 K temperature [identified also as Burn's temperature T_B; see inset (ii) in Fig. 1(b)]. These observed anomalies in structural parameters can be understood as follows. Ferroelectric order overcomes the decrease in anharmonic lattice phonon vibration and results in dilatation of the cubic lattice parameter; this effect is termed as spontaneous volume ferroelectrostriction (SVFS) [27]. Here, in the cubic phase the temperature behavior of the observed volume V_{exp} is found to deviate at ~477 K from its usual behavior V_{nm}. The SVFS is calculated by using the equation $\omega_s = [(V_{\text{exp}} - V_{nm})/V_{nm}] \times 100\%$ from Refs. [27,28] shown in inset (ii) in Fig. 2(b). Evolution of SVFS just below T_B [~477 K; inset (ii) in Fig. 2(b)] signifies the onset of polarization and also clearly indicates the existence of PNRs [8,27,28].

Motivated by the above-discussed results about evidence of PNRs, now we try to figure out the interplay between the Zr local structure and the PNRs. The Zr local structure

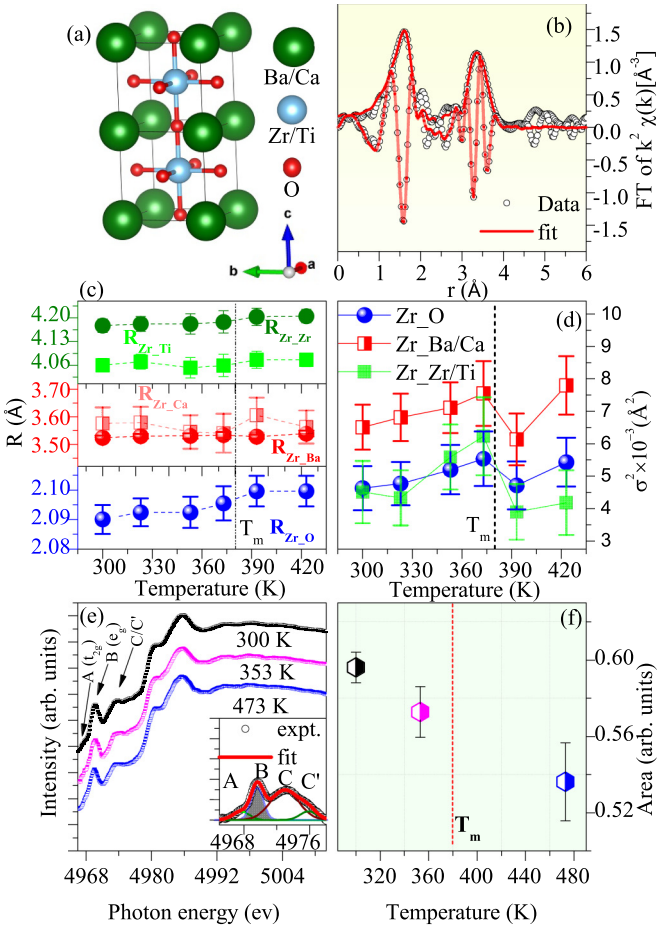

FIG. 3. (a) Standard perovskite model, which is used in the EXAFS fit. (b) Data and fit of the modulus and imaginary part of the Fourier transform in r space at room temperature. (c) Temperature-dependent coordination distances and (d) mean-square relative displacement parameters involved in the fitting of the Zr K-edge EXAFS. (e) The Ti K-edge XANES spectra at different temperatures; the inset shows the fitting of the preedge peak at room temperature. (f) Temperature dependence of the integrated intensity of feature B e_g in (e).

is investigated by performing the Zr K-edge EXAFS measurements at selected temperatures across T_m, and the results are shown in Fig. 3. We have used the standard perovskite model [see Fig. 3(a)] with linear Zr-O-Zr, Zr-O-Ti links during fitting, which was used earlier in BZT compositions [29]. During temperature-dependent EXAFS analysis we utilized the stoichiometric ratios of Ba/Ca and Ti/Zr obtained from the fit at 300 K, which are found near nominal composition values (see details of the EXAFS analysis in [23]). The fitted Zr K-edge EXAFS spectra at room temperature are shown in Fig. 3(b). From the results of the first coordination shell we found that the Zr-O bond distance increases significantly with temperature [see Fig. 3(c)]. The Zr-Ba and Zr-Ca interatomic distances are not the same at room temperature. As temperature increases, the parameters R_{Zr-Ba} and R_{Zr-Ca} get closer, while approaching T_m. The Zr-Ba interatomic distance (∼3.54 Å) is found to be significantly lower than the one in $BaZrO_3$ (∼3.64 Å) [30]; that is, the ZrO_6 octahedra are not in an ideal cubic environment. Additionally, the Ti-O bond distance (∼1.97 Å) is found to be shorter than the Zr-O bond distance (∼2.09 Å). In order to better understand the local picture, we turn our attention to the mean-square relative displacement (msrd) parameter as it contains information about thermal disorder as well as the static disorder of all scattering paths involved. Figure 3(d) shows evolution of the msrd (σ^2_{Zr-O}) with temperature. σ^2_{Zr-O} at room temperature is higher in this system compared to that of $BaZrO_3$ [30]. So, here, the Zr-O bonds contain an additional disorder other than thermal disorder (Einstein's model) [31,32]. Earlier [30], in the case of $BaZr_xTi_{1-x}O_3$, the presence of a temperature-independent static disorder together with thermal disorder was attributed to the distortion of ZrO_6 octahedra or tiny displacement of the Zr atoms. Additionally, at $\sim T_m$, σ^2_{Zr-O} shows an anomaly which was not seen earlier in the case of BZT. Again, below T_m the behavior of $\sigma^2_{Zr-Ti/Zr}$ with temperature is steeper than that of σ^2_{Zr-O} and $\sigma^2_{Zr-Ba/Ca}$. This behavior indicates modifications in linkage between the Zr-O and O-Ti bonds due to the decreasing covalent character of the Ti-O bonds. This modification is supported by direct evidence of decreasing hybridization between Ti and O with temperature seen in the Ti K-edge XANES spectra [see Figs. 3(e) and 3(f)]. Features A and B in Fig. 3(e) are ascribed to t_{2g} and e_g, respectively, and C/C' correspond to the local Zr/Ti ratio surrounding the absorber atom. The intensity of feature B e_g, which is related to Ti-O hybridization, decreases with temperature [Fig. 3(f)], confirming that with increasing temperature in this range the strength of the Ti-O hybridization weakens. Above T_m, $\sigma^2_{Zr-Ti/Zr}$ is more stable than other msrd parameters. Such temperature evolution of $\sigma^2_{Zr-Ti/Zr}$ suggests disorder along the Zr-O-Ti links, which delays phonon activation. At around T_m, σ^2_{Zr-O} also shows an anomaly, indicating direct involvement of the Zr local structure in polarization. Based on our results from local structural analysis and the dynamic neutron pair distribution function results from Pramanick *et al.* [21] we can say that the presence of Zr affects the surrounding Ti ions with its tensile stress and can change the polarization (by slowing down the dynamics of Ti^{4+} ions).

In order to understand the effect of these local structural heterogeneities on long-range polar order below T_m we also performed the dielectric measurements on the poled sample and compared the results with that of the unpoled sample. The dielectric dispersion or difference in permittivity at two frequencies is a measure of the degree of polar heterogeneity in a system [33,34]. In general, the dielectric dispersion is lesser for long-range ferroelectric materials, and it will be more for materials that show relaxor ferroelectric behavior, which are complex perovskite (ABO_3) systems with different cations present in the same site (A or B site). Relaxor ferroelectrics (i.e., $(Bi_{1/2}Na_{1/2})TiO_3$, $(1-x)(Bi_{1/2}Na_{1/2})TiO_3$-$x(Bi_{1/2}K_{1/2})TiO_3$ etc.) or canonical relaxors (i.e. PMN, PZN) can be transformed into long-range polar order by the application of sufficiently high electric field; therefore, dielectric dispersion and polar heterogeneity decrease. As we see from EXAFS results that the studied composition exhibits significant disorder because different size cations are present at both the A and B sites, a comparison of the dielectric dispersion in poled and unpoled samples

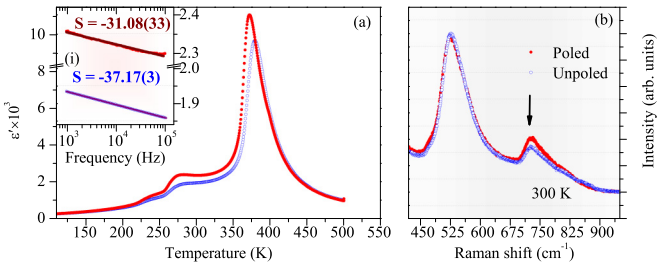

FIG. 4. (a) Temperature-dependent dielectric permittivity of poled and unpoled samples (at 1 kHz) taken during heating cycles. The inset shows the linearly fitted dielectric dispersion of poled and unpoled samples at room temperature. (b) Raman spectra (vertically translated for overlapping) of poled and unpoled samples at room temperature.

can directly reveal information about the degrees of polar heterogeneities. The inset in Fig. 4(a) shows that the dielectric dispersion decreases for the poled sample; therefore, it is inferred that the degree of polar heterogeneity is reduced after poling. These observations of the presence of polar heterogeneities in the unpoled sample can be correlated to structural heterogeneities observed in the EXAFS experiment.

Surprisingly, dielectric permittivity enhances in the case of the poled sample, which can be clearly seen from Fig. 4(a). Generally, by applying electric field to ferroelectric domains, polarization coherence increases along the field direction, and the sample becomes less susceptible to smaller ac field, and thereby dielectric permittivity decreases [35,36]. The same is true in the case of canonical relaxors (PMN, PZN) [37] or in the nonergodic phase of relaxor ferroelectrics (e.g. BNT-based systems) below T_m [34,38]. However, field induced real permittivity enhancement is reported to exist below T_m in the case of PMN-PT, and that has been attributed to synergistic interaction among ferroelectric domains and PNRs [39], which may be the case here too. We also performed Raman measurements on the poled and the unpoled samples [see Fig. 4(b)]. The Raman spectra of these samples match well with the previous reports [40–42]. The Raman spectra of this sample and other samples of the BZT-xBCT series ($x = 0.3$, 0.5, 0.6, 0.7) are compared and presented in the Supplemental Material [23]. The Raman mode at $\sim$522 cm^{-1} (see Fig. 4(b) and also Fig. S4 in [23]) has dominant A_1(TO) behavior and is related to BO_6 octahedra [43]. The Raman mode A_1(LO)/E(LO) at $\sim$720 cm^{-1} is the key signature related to the long-range ferroelectricity [44,45]. Both of these modes are present in all $BaTiO_3$-based systems. The intensity of the Raman mode (at $\sim$720 cm^{-1}) increases after poling and suggests that long-range ferroelectricity has, indeed, been enhanced after poling [43,44]. Therefore, both these measurements (dielectric and Raman) clearly suggest that nanoscale polar inhomogeneities exist along with long-range ferroelectricity below T_m and decrease marginally in poled sample.

In order to visualize effect of the local structural heterogeneities on ferroelectric domains (if any) we have also performed imaging by PRFM. PRFM is a technique based on the detection of the local converse piezoelectric effect, which is promising for imaging fine-scale domains [46–48]. Figure 5(a) shows the surface morphology of the polished sample by scanning a 2×2 μm^2 region. Figures 5(b) and 5(c) show the piezoelectric amplitude and PRFM phase of the same scanned region. Ferroelectric domains of different

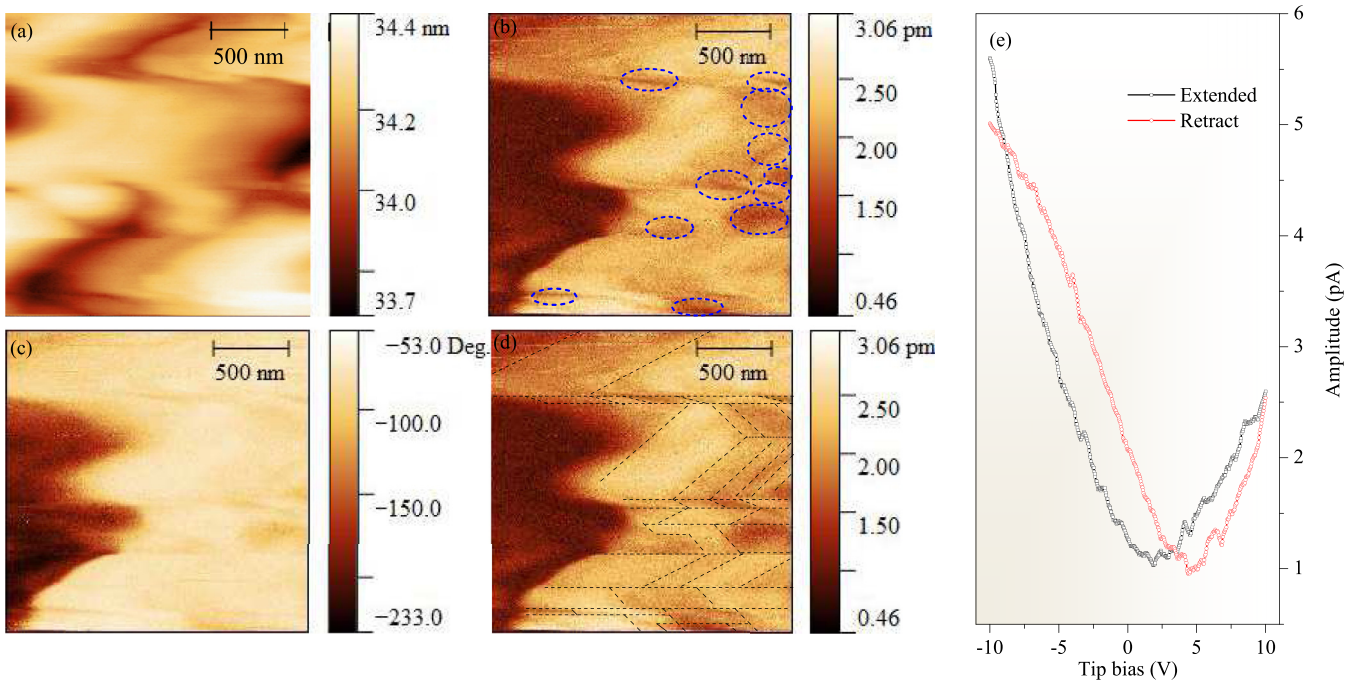

FIG. 5. (a) Topography, (b) piezoelectric amplitude, and (c) PRFM phase images of the same 2×2 μm^2 scan area at room temperature. The circles in (b) indicate different nanoscale domains. (d) Hierarchy of domains and subdomains marked by dashed lines and (e) local PRFM amplitude hysteresis loop with electric field.

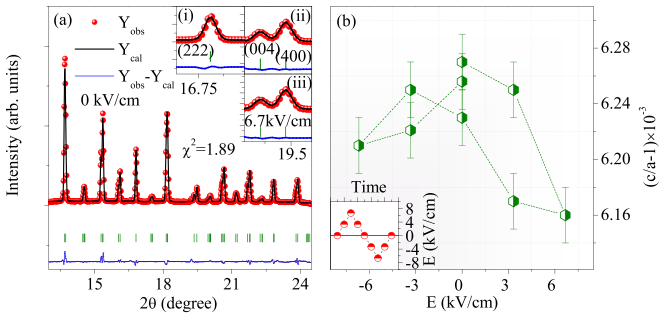

FIG. 6. (a) Rietveld refined x-ray diffraction pattern at zero electric field at room temperature. Insets (i) and (ii) in (a) show zoomed singlet $(222)_{pc}$ and doublet $(400)_{pc}$ peaks at zero field, and inset (iii) shows doublet $(400)_{pc}$ peak at 6.67 kV/cm. (b) Tetragonal distortion vs electric field shows an inverted butterflylike feature. A bipolar electric field was applied as shown in the inset of (b).

orientations with different contrasts can clearly be seen in Figs. 5(b) and 5(c). Nanoscale domain configurations (marked by circles) are observed for this composition within the large ferroelectric domain [see Fig. 5(b)]. Figure 5(d) shows the hierarchical domain configuration and is similar to the earlier reports resulting from the interplay of stress accommodation and polarization compensation [49–52]. Figure 5(e) shows the piezoelectric amplitude hysteresis loop which was obtained by applying electric field along the tip axis on the selected region. The butterfly-like piezoelectric amplitude hysteresis loop confirms the existence of well-defined polarization along the field direction. Historically, high piezoresponse has always been associated with hierarchical domain structure or complex microstructure with a combination of microdomains and nanodomains as these domains can easily respond to the external stimulus [50,53,54]. The complex domain configuration of this sample is compatible with its high piezoresponse (∼223 pC/N) [53,54].

Finally, for the sake of completeness we carried out x-ray diffraction (at ∼300 K, below T_m) in the presence of field up to ±6.7 kV/cm (∼1.67E_c) and quantified the structural changes under electric field. Electric field was applied on the sample at an angle of 45° with respect to the incident x-ray beam. This filters out effects of ferroelastic domain induced texturing and also ensures the reliability of the structural information through the Rietveld refinement [55]. Figure 6(a) shows the fitted XRD pattern, which is in good agreement with the experimental data. Figure 6(b) shows tetragonal distortion with electric field, although it is small. The observed tetragonal distortion reduction clearly indicates the electric field induced 90° domain wall motion by reduction of the anisotropy. In the Pb-based compositions, tetragonal distortion decreases with the enhancement of the monoclinic phase fraction [55–57]. However, in the present case no traces of monoclinicity are observed. Zoomed portions around (004) and (400) under the highest electric field are depicted in inset (iii) of Fig. 6(a), and no extra features are observed, which is the case in Pb-based compounds. Our electric field dependent XRD results and conclusions are well in agreement with those already reported for the same composition [5,58].

IV. DISCUSSION

BZT-60BCT is found to exhibit a weaker dielectric dispersion at around T_m compared to the canonical relaxors PMN and PZN; however, other characteristics of the relaxor type exist, e.g., a temperature of the real permittivity maxima (∼380 K) significantly higher than that of the imaginary permittivity maxima (∼375 K), deviation from the Curie-Weiss (C-W) law at a temperature (at ∼477 K) much higher than T_m, and the presence of a slim hysteresis loop [23] above T_m. The diffusion exponent of this system ($\gamma = 1.52$) suggests that this system exhibits a diffused ferroelectric phase transition, an intermediate between the classical ferroelectric ($\gamma = 1$) and canonical relaxor ($\gamma = 2$) [59]. Therefore, this system is analogically similar to PMN-PT and PZN-PT compositions near the MPB [39,60]. The dielectric anomalies (deviation from the C-W law and structural phase transition around T_m) are successfully justified by temperature-dependent XRD. The appearance of SVFS at ∼477 K which is associated with the onset of the PNRs is in accordance with other perovskite (ABO_3) ferroelectrics [27] in which polarization developments also take place due to the relative displacements of the cations and anions.

The origin of nanodomains here may relate to the inhomogeneities in the local structure and in strain (cations with different sizes) which break the long-range polar order. The compositions studied here are perfect for such a scenario because these are highly disordered compound as these involve Zr^{4+} (ionic radii $r \sim 0.72$ Å) substitution in place of Ti^{4+} ($r \sim 0.61$ Å) and Ca^{2+} ($r \sim 1.34$ Å) in place of Ba^{2+} ($r \sim 1.61$ Å) and thus large ionic radii [61] differences at both sites. Weakening of long-range polar order as a function of the Zr and Ca content in these compositions is experimentally evidenced by our Raman measurements, for which we have compared the four different compositions of BZT-xBCT (x = 0.3, 0.5, 0.6, 0.7) [23]. The A_1(TO) phonon mode [43,44], related to polar Ti-O vibrations (at ∼270 cm^{-1}), clearly becomes weaker and broader for Ca^{2+}-rich BZT-BCT systems.

Unlike Pb-based relaxors in which Pb positional disorder plays an important role, in BZT-BCT it has been reported [42] that at the A site (Ba/Ca) there is no significant disorder. However, from our Zr local structural studies we have found a significant difference between R_{Zr-Ba} and R_{Zr-Ca}, which together with our Raman results highlights that the A site (Ba/Ca) also contributes to local structural heterogeneities. Recent first-principles studies [62,63] also highlighted the steric effect induced B-site to A-site ferroelectricity transformation by incorporating lower ionic radii Ca in Ba sites. However, to shed light on the peculiar role of Ca more experimental investigations are necessary.

In PZT ceramics relaxor behavior is absent, although the same Ti and Zr cations are present in the B sites as in BZT. This is mainly because the A site cations possess a contrasting character. The stereochemically active lone pairs of Pb in covalently bonded Pb-O result in large off centering in their respective oxygen dodecahedra, whereas ionic-type bonding between Ba and O results in almost no shifting of Ba. In Pb-based systems, Pb positional disorder couples differently with different BO_6 octahedra; strong correlations between the cations make $PbTiO_3$ ferroelectric and $PbZrO_3$ antiferroelectric [64–66].

In BZT-BCT, substitution of Ca at the Ba sites, however, increases the A site bond strain due to a large ionic radius mismatch between Ba and Ca; however, the effect of Ca on the BO_6 octahedra is not as prominent as that of Pb. In $BaTiO_3$-based systems ($BaTiO_3$, $BaZr_xTi_{1-x}O_3$, $BaSn_xTi_{1-x}O_3$) polarization appears mainly due to Ti^{4+}, and the effect of dopant ions in the $BaTiO_3$ system exhibits diffuse scattering by setting up random strain fields generating frustrated PNRs [19], whereas PZT does not show diffuse scattering [67]. Moreover, in $BaTiO_3$-based relaxors B site substitution has a more important role in setting up local strains by decreasing transverse correlations and creating frustration during long-range polar order [19]. Fanoresonance and the thermally activated terahertz relaxation mode [68] due to the difference in off centering of Zr^{4+} and Ti^{4+} are attributed as the cause of PNRs or relaxor behavior in BZT [69]. The Ti^{4+} dynamics are reported to exist even in the nonergodic relaxor phase of BZT [70,71].

Generally, for nonergodic relaxors (below T_m) dielectric dispersion is larger (compare to long-range ferroelectrics), and application of a sufficiently high electric field results in a reduction of dielectric dispersion. Dispersion in the permittivity data signifies the degree of polar inhomogeneity [33,34]. Here, in this system, dispersion in the real permittivity is also present well below T_m. The slopes calculated from dielectric permittivity variation with frequency [inset in Fig. 4(a)] suggest that significant polar inhomogeneity is present in the case of the unpoled specimen, and it decreases only marginally after electric poling [23]. Normally, the presence of PNRs below T_m is expected to show nonergodicity [16], and application of electric field results in the reduction of real permittivity, which here is counterintuitive [34]. Further, both PNRs and ferroelectric domains individually are reported to show enhancement of polarization coherence after poling and thereby a reduction in the dielectric constant [36,72,73]. In contrary, Li *et al.* [39] highlighted dielectric constant enhancement after poling as the cornerstone of ultrahigh piezoelectricity. The temperature evolution of structural transformations of PNRs at lower temperature and colinear arrangement of PNRs at higher temperature were attributed to dielectric as well as piezoamplification in PNR-ferroelectric composites [39]. In our case also, in the poled sample real permittivity increases significantly (∼23%). We speculate that similar kinds of interactions are involved in this system, as explained by Li *et al.* [39]. Our PRFM measurements show the presence of polar nanodomains at room temperature and support our conjecture.

V. CONCLUSIONS

In summary, by combining a set of local and average structural studies on a tetragonal BZT-BCT ceramic we have presented the relationship between local structural heterogeneities in it and its macroscopic dielectric, ferroelectric, and piezoelectric properties. Temperature-dependent XRD confirms a tetragonal to cubic phase transition at $\sim T_m$ (380 K). Furthermore, the onset of spontaneous volume ferroelectrostriction and deviation from the C-W law (at $T_B \sim 477$ K), slim hysteresis, and dielectric dispersion confirm the presence of PNRs below 477 K in this composition. The Zr local structural investigations confirm that the ZrO_6 and TiO_6 octahedra retain the individuality of their respective parent compounds (i.e., $BaZrO_3$ and $BaTiO_3$), and ZrO_6 octahedra are found to have direct involvement during polarization development. The larger ZrO_6 octahedra create tensile stress on surrounded TiO_6 octahedra, and the presence of static disorder in Zr-O bonds produces local structural heterogeneities; during polarization development the ZrO_6 octahedra distort. Local structural heterogeneities try to break the long-range polar order by forming nanoscale hierarchical domains. These domains are evidenced by PRFM and are supposed to be responsible for the enhancement of real permittivity (∼23%) after poling. Additionally, high-resolution synchrotron XRD confirms also the electric field induced reduction of tetragonal distortion in this ceramic.

ACKNOWLEDGMENTS

K.D., A.A., and D.K.S gratefully acknowledge the financial support from the Department of Science and Technology (DST) in India through the India-DESY collaboration for performing experiments at PETRA-III, DESY. The authors acknowledge S. Yadav for help with P-E loop measurements and A. Yadav for help with EXAFS data analysis. D. Reuther is acknowledged for setting up the voltage source used in the electric field dependent XRD measurements. C.R. acknowledges the support from the project CALIPSOplus under Grant Agreement No. 730872 from the EU Framework Programme for Research and Innovation Horizon 2020.

[1] W. Liu and X. Ren, Phys. Rev. Lett. **103**, 257602 (2009).
[2] Y. Nahas, A. Akbarzadeh, S. Prokhorenko, S. Prosandeev, R. Walter, I. Kornev, J. Íñiguez, and L. Bellaiche, Nat. Commun. **8**, 15944 (2017).
[3] J. Gao, Y. Dai, X. Hu, X. Ke, L. Zhong, S. Li, L. Zhang, Y. Wang, D. Wang, Y. Wang *et al.*, Europhys. Lett. **115**, 37001 (2016).
[4] J. Gao, X. Hu, L. Zhang, F. Li, L. Zhang, Y. Wang, Y. Hao, L. Zhong, and X. Ren, Appl. Phys. Lett. **104**, 252909 (2014).
[5] G. Tutuncu, B. Li, K. Bowman, and J. L. Jones, J. Appl. Phys. **115**, 144104 (2014).
[6] K. Brajesh, K. Tanwar, M. Abebe, and R. Ranjan, Phys. Rev. B **92**, 224112 (2015).
[7] K. Brajesh, M. Abebe, and R. Ranjan, Phys. Rev. B **94**, 104108 (2016).
[8] L. E. Cross, Ferroelectrics **76**, 241 (1987).
[9] M. E. Manley, D. L. Abernathy, R. Sahul, D. E. Parshall, J. W. Lynn, A. D. Christianson, P. J. Stonaha, E. D. Specht, and J. D. Budai, Sci. Adv. **2**, e1501814 (2016).
[10] S.-E. Park and T. R. Shrout, J. Appl. Phys. **82**, 1804 (1997).
[11] A. Bokov and Z.-G. Ye, J. Mater. Sci. **41**, 31 (2006).
[12] G. Burns and F. Dacol, Solid State Commun. **48**, 853 (1983).
[13] C. Perrin, N. Menguy, E. Suard, C. Muller, C. Caranoni, and A. Stepanov, J. Phys.: Condens. Matter **12**, 7523 (2000).
[14] P. S. Halasyamani, Chem. Mater. **16**, 3586 (2004).
[15] R. Pirc and R. Blinc, Phys. Rev. B **76**, 020101(R) (2007).

[16] A. A. Bokov and Z.-G. Ye, J. Adv. Dielectr. **2**, 1241010 (2012).
[17] A. Simon and J. Ravez, Ferroelectrics **240**, 1601 (2000).
[18] Y. Huang, C. Zhao, B. Wu, and J. Wu, ACS Appl. Mater. Interfaces **12**, 23885 (2020).
[19] Y. Liu, R. Withers, B. Nguyen, and K. Elliott, Appl. Phys. Lett. **91**, 152907 (2007).
[20] L. Xie, Y. L. Li, R. Yu, Z. Y. Cheng, X. Y. Wei, X. Yao, C. L. Jia, K. Urban, A. A. Bokov, Z.-G. Ye, and J. Zhu, Phys. Rev. B **85**, 014118 (2012).
[21] A. Pramanick, W. Dmowski, T. Egami, A. S. Budisuharto, F. Weyland, N. Novak, A. D. Christianson, J. M. Borreguero, D. L. Abernathy, and M. R. V. Jørgensen, Phys. Rev. Lett. **120**, 207603 (2018).
[22] A. Akbarzadeh, K. Brajesh, Y. Nahas, N. Kumar, S. Prokhorenko, D. Swain, S. Prosandeev, R. Walter, I. Kornev, J. Íñiguez, B. Dkhil, R. Ranjan, and L. Bellaiche, Phys. Rev. B **98**, 104101 (2018).
[23] See Supplemental Material at http://link.aps.org/supplemental/10.1103/PhysRevB.103.L100205 for details about the structural characterization, P-E hysteresis measurements, dielectric and diffusion exponents in the poled sample, Raman spectra, and EXAFS analysis.
[24] G. Burns and F. H. Dacol, Phys. Rev. B **28**, 2527 (1983).
[25] A. A. Bokov, Y.-H. Bing, W. Chen, Z.-G. Ye, S. A. Bogatina, I. P. Raevski, S. I. Raevskaya, and E. V. Sahkar, Phys. Rev. B **68**, 052102 (2003).
[26] J. Rodríguez-Carvajal, FULLPROF. A Rietveld Refinement and Pattern Matching Analysis Program (Laboratoire Leon Brillouin (CEA-CNRS), France, 2000).
[27] J. Chen, L. Hu, J. Deng, and X. Xing, Chem. Soc. Rev. **44**, 3522 (2015).
[28] J. Chen, F. Wang, Q. Huang, L. Hu, X. Song, J. Deng, R. Yu, and X. Xing, Sci. Rep. **3**, 2458 (2013).
[29] I. Levin, E. Cockayne, V. Krayzman, J. C. Woicik, S. Lee, and C. A. Randall, Phys. Rev. B **83**, 094122 (2011).
[30] C. Laulhé, F. Hippert, J. Kreisel, M. Maglione, A. Simon, J. L. Hazemann, and V. Nassif, Phys. Rev. B **74**, 014106 (2006).
[31] P. Fornasini and R. Grisenti, J. Synchrotron Radiat. **22**, 1242 (2015).
[32] G. Beni and P. Platzman, Phys. Rev. B **14**, 1514 (1976).
[33] P. B. Groszewicz, M. Gröting, H. Breitzke, W. Jo, K. Albe, G. Buntkowsky, and J. Rödel, Sci. Rep. **6**, 31739 (2016).
[34] G. D. Adhikary, D. K. Khatua, A. Senyshyn, and R. Ranjan, Phys. Rev. B **99**, 174112 (2019).
[35] P. Yadav, S. Sharma, and N. Lalla, J. Appl. Phys. **121**, 184101 (2017).
[36] K. C. Koa, *Dielectric Phenomena in Solids with Emphasis of Physical Concepts of Electronic Processes* (Elsevier Academic Press, Amsterdam, 2004).
[37] Y. Zhang, J. Tian, L. Li, and Z. Gui, J. Mater. Sci.: Mater. Electron. **11**, 347 (2000).
[38] B. N. Rao, R. Datta, S. S. Chandrashekaran, D. K. Mishra, V. Sathe, A. Senyshyn, and R. Ranjan, Phys. Rev. B **88**, 224103 (2013).
[39] F. Li, S. Zhang, T. Yang, Z. Xu, N. Zhang, G. Liu, J. Wang, J. Wang, Z. Cheng, Z.-G. Ye *et al.*, Nat. Commun. **7**, 13807 (2016).
[40] L. Zhang, M. Zhang, L. Wang, C. Zhou, Z. Zhang, Y. Yao, L. Zhang, D. Xue, X. Lou, and X. Ren, Appl. Phys. Lett. **105**, 162908 (2014).
[41] G. Singh, V. Sathe, and V. Tiwari, J. Electron. Mater. **46**, 4976 (2017).
[42] K. Datta, K. Brajesh, R. Ranjan, and B. Mihailova, Phys. Rev. B **102**, 060102(R) (2020).
[43] V. Buscaglia, S. Tripathi, V. Petkov, M. Dapiaggi, M. Deluca, A. Gajović, and Y. Ren, J. Phys.: Condens. Matter **26**, 065901 (2014).
[44] B. C. Keswani, D. Saraf, S. Patil, A. Kshirsagar, A. James, Y. Kolekar, and C. Ramana, J. Appl. Phys. **123**, 204104 (2018).
[45] U. Pasha, H. Zheng, O. Thakur, A. Feteira, K. Whittle, D. Sinclair, and I. Reaney, Appl. Phys. Lett. **91**, 062908 (2007).
[46] H. Uršič and U. Prah, Proc. R. Soc. A **475**, 20180782 (2019).
[47] K. Kim and J. E. Huber, J. Eur. Ceram. Soc. **35**, 1459 (2015).
[48] M. Otonicar, H. Ursic, M. Dragomir, A. Bradesko, G. Esteves, J. Jones, A. Bencan, B. Malic, and T. Rojac, Acta Mater. **154**, 14 (2018).
[49] J. Yao, W. Ge, L. Luo, J. Li, D. Viehland, and H. Luo, Appl. Phys. Lett. **96**, 222905 (2010).
[50] H. Wang, J. Zhu, N. Lu, A. Bokov, Z.-G. Ye, and X. Zhang, Appl. Phys. Lett. **89**, 042908 (2006).
[51] K. Fang, W. Jing, and F. Fang, J. Am. Ceram. Soc. **102**, 7710 (2019).
[52] J. Yao, L. Yan, W. Ge, L. Luo, J. Li, D. Viehland, Q. Zhang, and H. Luo, Phys. Rev. B **83**, 054107 (2011).
[53] C. Hu, X. Meng, M.-H. Zhang, H. Tian, J. E. Daniels, P. Tan, F. Huang, L. Li, K. Wang, J.-F. Li *et al.*, Sci. Adv. **6**, eaay5979 (2020).
[54] A. Khachaturyan, Philos. Mag. **90**, 37 (2010).
[55] M. Hinterstein, J. Rouquette, J. Haines, P. Papet, M. Knapp, J. Glaum, and H. Fuess, Phys. Rev. Lett. **107**, 077602 (2011).
[56] R. Guo, L. E. Cross, S.-E. Park, B. Noheda, D. E. Cox, and G. Shirane, Phys. Rev. Lett. **84**, 5423 (2000).
[57] H. Liu, J. Chen, L. Fan, Y. Ren, Z. Pan, K. V. Lalitha, J. Rödel, and X. Xing, Phys. Rev. Lett. **119**, 017601 (2017).
[58] M. C. Ehmke, N. H. Khansur, J. E. Daniels, J. E. Blendell, and K. J. Bowman, Acta Mater. **66**, 340 (2014).
[59] D. Nuzhnyy, J. Petzelt, M. Savinov, T. Ostapchuk, V. Bovtun, M. Kempa, J. Hlinka, V. Buscaglia, M. T. Buscaglia, and P. Nanni, Phys. Rev. B **86**, 014106 (2012).
[60] O. Noblanc, P. Gaucher, and G. Calvarin, J. Appl. Phys. **79**, 4291 (1996).
[61] R. D. Shannon, Acta Cryst. A **32**, 751 (1976).
[62] D. Amoroso, A. Cano, and P. Ghosez, Phys. Rev. B **97**, 174108 (2018).
[63] D. Amoroso, A. Cano, and P. Ghosez, Appl. Phys. Lett. **114**, 092902 (2019).
[64] Y. Kuroiwa, S. Aoyagi, A. Sawada, J. Harada, E. Nishibori, M. Takata, and M. Sakata, Phys. Rev. Lett. **87**, 217601 (2001).
[65] A. K. Tagantsev, K. Vaideeswaran, S. B. Vakhrushev, A. V. Filimonov, R. G. Burkovsky, A. Shaganov, D. Andronikova, A. I. Rudskoy, A. Q. R. Baron, H. Uchiyama *et al.*, Nat. Commun. **4**, 2229 (2013).
[66] D. Cao, I.-K. Jeong, R. H. Heffner, T. Darling, J.-K. Lee, F. Bridges, J.-S. Park, and K.-S. Hong, Phys. Rev. B **70**, 224102 (2004).
[67] D. Phelan, C. Stock, J. A. Rodriguez-Rivera, S. Chi, J. Leão, X. Long, Y. Xie, A. A. Bokov, Z.-G. Ye, P. Ganesh *et al.*, Proc. Natl. Acad. Sci. USA **111**, 1754 (2014).
[68] D. Wang, J. Hlinka, A. Bokov, Z.-G. Ye, P. Ondrejkovic, J. Petzelt, and L. Bellaiche, Nat. Commun. **5**, 5100 (2014).

[69] A. R. Akbarzadeh, S. Prosandeev, E. J. Walter, A. Al-Barakaty, and L. Bellaiche, Phys. Rev. Lett. **108**, 257601 (2012).

[70] J. Petzelt, D. Nuzhnyy, M. Savinov, V. Bovtun, M. Kempa, T. Ostapchuk, J. Hlinka, G. Canu, and V. Buscaglia, Ferroelectrics **469**, 14 (2014).

[71] J. Petzelt, D. Nuzhnyy, V. Bovtun, M. Kempa, M. Savinov, S. Kamba, and J. Hlinka, Phase Trans. **88**, 320 (2015).

[72] F. Li, S. Zhang, Z. Xu, and L.-Q. Chen, Adv. Funct. Mater. **27**, 1700310 (2017).

[73] F. Li, S. Zhang, D. Damjanovic, L.-Q. Chen, and T. R. Shrout, Adv. Funct. Mater. **28**, 1801504 (2018).